Electron density and two-channel neutron emission measurements in steady-state spherical inertial-electrostatically confined plasmas, with review of the 1-D kinetic model

Chris C. Dobson
Propulsion Research Center, NASA/Marshall Space Flight Center, Huntsville, Alabama 35812

Ivana Hrbud
Purdue University, School of Aeronautical and Astronautical Engineering, West Lafayette, Indiana 47906-2023

(ABSTRACT:) Electron density measurements have been made in steady-state plasmas in a spherical inertial electrostatic confinement (IEC) discharge using microwave interferometry. Plasma cores interior to two cathodes, having diameters of 15 and 23 cm, respectively, were probed over a transverse range of 10 cm with a spatial resolution of about 1.4 cm for buffer gas pressures from 0.2 to 6 Pa in argon and deuterium. The transverse profiles are generally flat, in some cases with eccentric symmetric minima, and give mean densities of from ≈ 0.4 to 7×10^{10} cm^{-3}, the density generally increasing with the neutral gas pressure. Numerical solutions of the 1-D Poisson equation for IEC plasmas are reviewed and energy distribution functions are identified which give flat transverse profiles. These functions are used with the plasma approximation to obtain solutions which also give densities consistent with the measurements, and a double potential well solution is obtained which has minima qualitatively similar to those observed. Explicit consideration is given to the compatibility of the solutions interior and exterior to the cathode, and to grid transparency. Deuterium fusion neutron emission rates were also measured and found to be isotropic, to within the measurement error, over two simultaneous directions. Anisotropy was observed in residual emissions during operation with non-fusing hydrogen-1. The deuterium rates are consistent with predictions from the model.

I. INTRODUCTION

The inertial electrostatic confinement (IEC) of plasma was originally conceived as a method for producing controlled nuclear fusion. It is of research interest in the production of high-energy neutrons[1-6] and other particles[7] and in the study of plasma dynamics,[3, 8-18] as well as in the production of energy.[19-24] As a neutron source, IEC is of interest in detection, imaging and research applications, including assaying and tomography,[1, 4] and has been proposed for the engineering of sub-critical fission reactors.[5] The rate of fusion energy production as a fraction of input power of these devices is typically of order 10^{-9},[1, 2, 4, 19, 20, 25-27] with values up to ~10^{-5} reported.[19] In an (ion-injected) IEC plasma, the ions travel in radial trajectories and circulate through an open spherical, or cylindrical, cathode, and the electrons circulate interior to the cathode. The radial distribution of density, particularly interior to the cathode, which results from these motions is of key significance to the fusion and more generally to the plasma dynamics. In some cases, there is experimental evidence of spatial oscillations in this density,[19, 28-30] and predictions of oscillations, in both the density and the electrostatic potential, have played a seminal role in IEC research.

Electron density profiles from D_2 in a pulsed cylindrical IEC device were measured by Meeker, et al., using an intra-cavity laser heterodyne interferometer.[28] Densities from $\cong 0.3$ to 8×10^{11} cm^{-3} were measured, integrated over a path of 20 cm, and spatial oscillations in excess of 30% the mean density were observed. In a previous, similar, experiment, Dolan, et al.,[13] using quasi-resonant interferometry of metastable neon atoms, determined a ceiling of 2×10^{11} cm^{-3} for the electron density and estimated specific values for this density based on a theoretical dependence of the metastable atom density on the electron density. Dolan, et al., also presented calculations of intra-cathode density and potential profiles using a 1-D kinetic model and found solutions predicting densities consistent with the neon experiments. These particular solutions used step function distributions of total energy and angular momentum, and the same basic model has been examined by other workers,[14, 17, 29, 31-33] using also delta-function distributions[14, 17, 19, 33] and quasi-thermal distributions,[17, 32] typically for the purpose of testing assumptions about the physics or for comparison with experiment.

We report here electron density measurements made in spherical steady-state IEC Ar and D_2 plasmas using microwave interferometry. The line-integrated, or areal, densities are from < 1 to $\cong 8 \times 10^{11}$ cm^{-2}, over paths of 15 and 23 cm, corresponding to uniform densities from $\cong 0.4$ to 7×10^{10} cm^{-3}. Transverse scans of the plasma over a distance of 10 cm were performed, and the resulting profiles are generally flat, with oscillatory structure evident in some of the data. The spatial resolution for these measurements was limited by the beam diameter to about 1.4 cm. By comparison, the laser heterodyne technique has a spatial

resolution of ≈ 1 mm, but is not amenable to steady-state discharges, and is perhaps less sensitive due to the short wavelength. In Sect. IV, calculations from the 1-D 2-species kinetic model are summarized and specific theoretical transverse profiles are compared with the measurements. A modified rectangular distribution function and the thermal equilibrium distribution are introduced, largely to produce flat central profiles, and explicit connection to the interelectrode region is made.

Measurements of the D-D fusion neutron production rate have also been made using a pair of calibrated ^{3}He detectors. The measured rates are consistent with rates reported in the literature[4, 25-27] and are compared with predictions from the model. The dual-channel configuration is used to quantify the neutron emission isotropy over two directions, and comparative studies using both H_2 and D_2 provide information on the cathode fusion contribution,[4] which is less isotropic. Both the electron density and the neutron emission measurements were made using two cathode diameters for a fixed anode.

II. EXPERIMENT

The IEC apparatus is comprised of a 60-cm diameter spherical vacuum chamber with an interior concentric cathode grid and supporting hardware. The vacuum chamber wall is grounded and forms the anode of the circuit, and voltage is applied with a 100-kV, 5 kW power supply. The voltage V_g and current I_S are measured independently of the

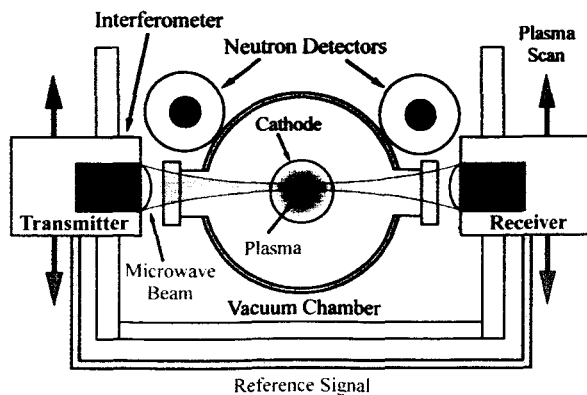(a) OPERATION (Side View)
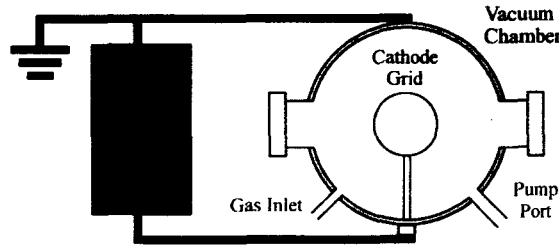
(b) MEASUREMENTS (Top View)

FIG. 1. Schematic of IEC device showing (a) basic configuration and (* add V and I meas.?; H20 in/out?) (b) microwave and He3 diagnostics.
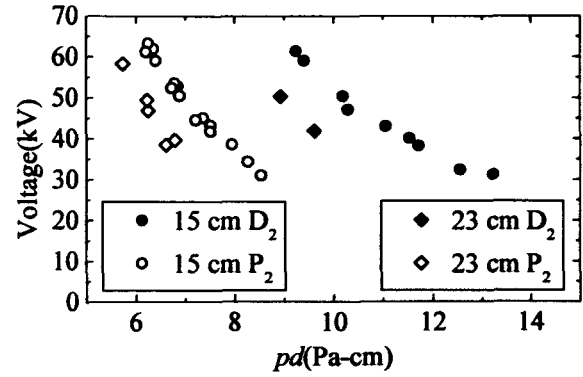

FIG. 2 IEC operating voltages as functions of the Paschen product pd for protium and deuterium using two cathodes.

supply using an external voltage divider and an integrated parametric current transformer, respectively. The flow of neutral gas through the chamber is controlled by a 0.1 slm MKS flow controller, and the chamber pressure p is set by the flow and pumping speeds. The chamber is double-walled and water is circulated through the inter-wall cavity for thermal regulation. This regulation was found to significantly enhance the stability of operation, particularly at high voltages. A schematic of the IEC device is given in Fig. 1a.

The cathode grid consists of 7 "great circle" stainless steel loops, which are pre-fabricated o-ring seals, welded together to form a symmetric lattice of triangles of two, similar, sizes. Two diameters, 15.2 and 22.9 cm, of cathodes of this design were used. In each case the wire loop cross sectional diameter is 0.0794 cm, resulting in geometric transparencies of 0.964 and 0.976, respectively, for the two cathode sizes. A second 15 cm grid design, based on "latitude" circles, was also used for some of the measurements. This "L-grid" consists of three great circle loops with mutually orthogonal axes, of which two loops are each flanked by symmetric pairs of smaller, coaxial, circles; the geometric transparency is $\cong 0.95$ (*).

The experiment was operated in discharge mode[20] so that the operating voltage is fixed by the neutral gas chamber pressure. Once breakdown has occurred, small changes in the voltage suffice to adjust the current over the full range of the power supply.[3] Argon and deuterium gases were used for the interferometry. Deuterium was used for the fusion work and hydrogen-1, or protium, was used for comparison with deuterium. The experimental conditions for these gases are in the large mean-free-path regime of the Paschen curve for breakdown voltage.[34] Fig. 2 gives Paschen data for the two cathode sizes for protium and deuterium, taken from experiments measuring neutron emission rates. The striking distance d is the interelectrode spacing,[3] and it is seen that the two cathodes fall on different curves.

The neutral gas particle density n_2 is required for the theoretical fusion reaction rates in Sect. V, as well as for calculation of the ionization fractions (Sect. VI), and the n_2 used here are taken from the pressure p assuming a nominal neutral temperature T_2. This temperature T_2 is generally higher than the ambient temperature T_{amb} and depends on the

fraction α of the electrical power $|V_g I_s|$ channeled into the net heating of the neutral gas. In particular, the change in temperature experienced by the neutral gas as it passes through the vacuum chamber is

$$\Delta T_2 = \alpha \frac{|V_g| I_s}{\dot{M} \beta k} \tag{1}$$

where $\dot{M}$ is the rate at which neutral particles enter (or leave) the chamber, known from the flow controller, β is a constant in the range of from 5/2 to 9/2, depending on the gas species and temperature, and k is the Boltzmann constant. The fraction α is not known, but unless it is very small, substantial heating will result; the value required for $\Delta T_2 \cong T_{amb}$ is $\alpha \cong 0.002$ for typical microwave data in Ar and $\alpha \cong 4 \times 10^{-5}$ for typical fusion data.

III. MICROWAVE INTERFEROMETRY

A three-frequency microwave interferometer was used to make electron density measurements in the IEC plasmas. Optical access is provided by a pair of opposed viewports in the equatorial plane of the vacuum chamber. These viewports have a clear aperture of 10 cm and the separation of the windows along the optical axis is approximately 76 cm. The windows were made of either alkali borosilicate (Corning 7056) glass or plexiglass. The transverse spatial distribution of the microwave beam irradiance is approximately Gaussian with a nominal 1.25 cm focal spot. The two microwave frequencies used for the IEC work were 70 and 90 GHz, and the full-width at half-maximum of the 70 GHz beam waist was measured to be 1.8 cm. The transverse scanning range for the microwave beam was 10 to 12 cm. Stepper motors were used both for the transverse scanning and for the phase calibration, which was performed by direct axial translation of the interferometer transmitter. A schematic of the microwave configuration is shown in Fig. 1b and further details are given in Ref. 35.

The interferometer was calibrated at each location in a transverse scan. Just prior to, or immediately following, the plasma measurement, the transmitter was translated axially over a range of about one fringe centered on the measurement position, which was chosen near a zero-crossing. The interferometer has quadrature capability and the data acquisition was performed off-quadrature, with shifts of < 55°, so that there were two useful channels of data at each transverse location, both of which were used in the data reduction. Also, in many cases, calibration scans were performed with the plasma present in the chamber for comparison and as a check. The axial scans were performed in discrete steps and the position of the transmitter was recorded at each step, and this resulted in typical calibration times of $\cong 100$ sec due to constraints on the polling speed for the stepper motor (the scan itself requires only a few seconds). The plasma measurements themselves were performed by cycling the plasma on and off several times, with each cycle having a duration of approximately 10 seconds, and the phase shifts were subsequently determined by averaging the data flanking the termination points in these cycles. The operation of the IEC discharge is stable over periods of many minutes, particularly at low voltages, and the restriction of the measurement time in this way was done largely to reduce the measurement error from drift in the interferometer signals.

A Monte Carlo error analysis was performed for the phase shift measurements, based on the individual calibration files and the measurement data itself.[35] The resulting error bar for the measurement of electron density, as presented here, represents an estimate of the unit width ($\sqrt{2}$ standard deviations) of a Gaussian distribution. This density error is generally substantial, as a fraction of the measurement value, due to the small phase shifts, which are typically of order 10^{-2} fringe.

Unlike the cylindrical case, the interferometer beam in spherical geometry necessarily has a radial component and the beam must pass through the cathode grid. In the present case, diffraction and absorption due to the grid are expected to be minor. The grid apertures are several centimeters in dimension, and the ratio of the diameter of the wire loops to the interferometer wavelength is < 0.24. In this connection it is of note that the microwave polarization was perpendicular to the transverse direction, so that any wire loop with an approximately transverse orientation, where it might have maximum effect, would tend to select for the beam polarization. In any case, any effect of the grid on the beam is present during calibration as well as during the measurements; also, trial data reductions using the calibrations made with the plasma present gave very similar results to those made in the absence of the plasma (apart from the sign of the phase shift).

The spatial resolution for the interferometry, set by the beam geometry, is taken to be 1.8 cm for the 70 GHz data, from the waist measurement, and 1.4 cm for the 90 GHz cases, from wavelength scaling and the manufacturer's specification. The wavelengths for these two beams are 0.429 and 0.333 cm, respectively, and thus there are transverse spatial gradients in the microwave irradiance on scales comparable to the wavelength. Moreover, there are potentially gradients in the electron density on scales comparable to the wavelength, due to intra-cathode radial structure. The effect of such density gradients on the microwave detector signals is generally difficult to calculate, particularly given the irradiance gradients, and in the data reduction here this effect is neglected based on the assumption that any error thus introduced is small in comparison to the phase shift error. The inferred phase shift is taken as proportional in the usual way to the line-integral of the density, i.e., to the product of the path length and the mean density in the volume occupied by the beam.

For the interferometry, the apparatus was operated with cathode voltages $\cong 1$ to 5 kV and power supply currents $\cong 50$ mA; neutral gas pressures were from $\cong 0.2$ to 6 Pa. Visually, the IEC plasma under these conditions typically manifests a fairly well defined core region with diameter comparable to, but less than, that of the cathode. Outside the cathode, the electron density is necessarily very low; e.g., for 50 mA of direct electron flow from the 15 cm cathode to anode at 1 kV, the mean density is $\cong 10^5$ cm^{-3}. Therefore, the

3

plasma may be considered as confined to the interior of the cathode.

Transverse profiles of the areal electron density N from the Ar plasmas are given in Fig. 3. These data were collected on several days over a period of a few months. The profiles are generally flat across the center of the plasma and have average densities of from $\cong 4$ to 8×10^{11} cm^{-2}. Most of the radial variation is comparable in magnitude to the measurement error, but there is a significant tendency toward eccentric symmetric minima in some cases. This is clearest in the standard 15 cm grid data, for which distinct minima are evident at $x \cong \pm 4$ cm. It should be noted that clipping of the microwave beam by the viewport aperture is present in some degree for most of the data. At ± 5 cm, where the beam is nominally bisected by the window edge, attenuation of the signal is $> 80\%$, and this is reflected in the error bars. The transverse step size was 0.635 cm, except for the L-grid data, most of which was taken with steps half this size. The 70
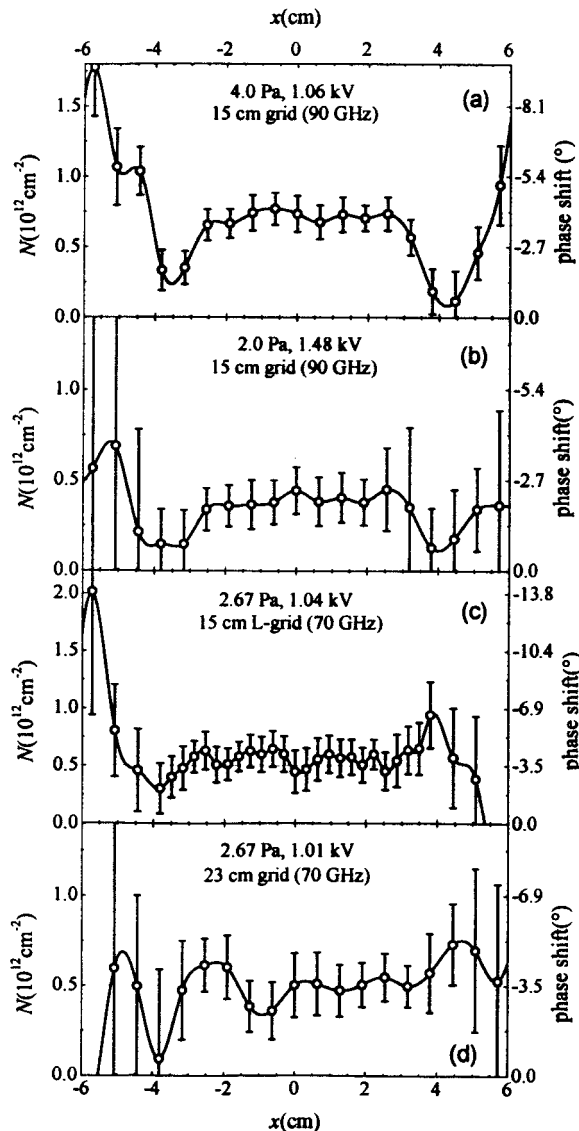
GHz microwave frequency is somewhat more sensitive to the density than the 90 GHz component, but the accuracy of the

FIG. 4. D_2 interferometer transverse scan data. The left axis gives areal electron density N in units of 10^{12} cm^{-2}, the right axis, phase shifts in degrees.

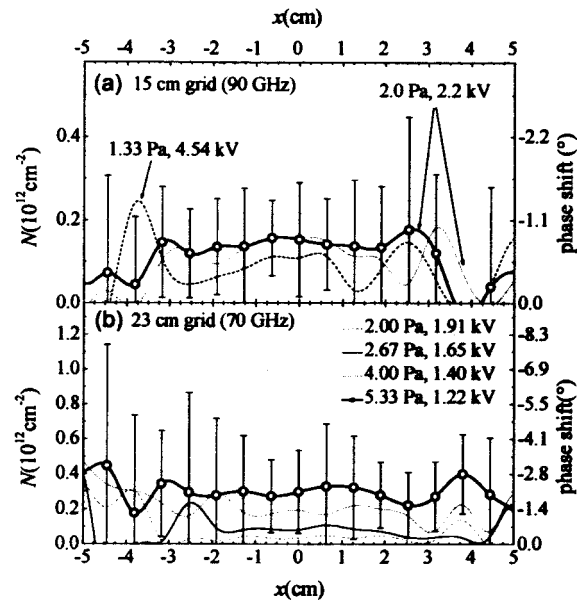FIG. 3. Ar interferometer transverse scan data. The left axis gives areal electron density N in units of 10^{12} cm^{-2}, the right axis, phase shifts in degrees.
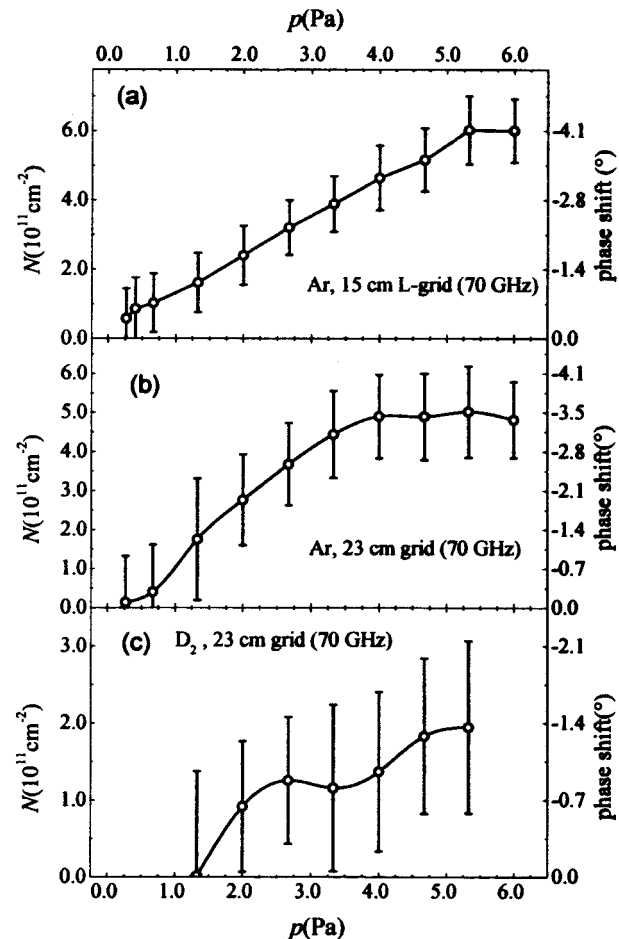
FIG. 5 Pressure scan data for the interferometer. The left axis gives areal electron density N in units of 10^{11} cm^{-2}, the right axis, phase shifts in degrees.

measurements is affected also by the signal strength and calibration quality. The transverse scan data for D_2, collected over a comparable time period, are presented in Fig. 4. These profiles are qualitatively similar to those in Ar, but the densities are distinctly smaller, in the range of from $\cong 0.7$ to 3×10^{11} cm^{-2}.

Pressure scans were also performed at the center location ($x = 0$). This data is given in Fig. 5. The electron density generally increases with neutral gas pressure, but there are indications of limiting densities at the higher pressures. This is clearest in the Ar data for the 23 cm grid, which shows a constant density in the range 4–6 Pa. This behavior is reminiscent of that of fusion rate density at lower pressures observed by Hirsch and Miley,[20] in which the fusion rate increases with increasing pressure only up to a point (about 1.3 Pa), and is discussed in Sect. VI.

For the purposes of comparison with the model in the following section, the essential features of the experimental transverse profiles are that (1) the areal densities are of order 10^{11} to 10^{12} cm^{-2}, (2) the densities are approximately constant in the center, giving flat profiles, and (3) some of the 15-cm grid data show minima in the densities at $x \cong \pm 4$ cm.

IV. STEADY-STATE 1-D KINETIC MODEL

The convention adopted here for the definition of space charge currents includes charges traveling in both radial directions, inward and outward,[13, 19] rather than in a single direction only;[14, 36] this total current corresponds directly to the number density of charge carriers, which drives the Poisson equation. In particular, the circulating ion current I_0 is related to the ion current collected by the cathode I_{IC} by[37]

$$\frac{I_0}{I_{IC}} = \frac{2\gamma_e}{1-\gamma_e^2}, \tag{2}$$

where γ_e is the effective cathode grid transparency. γ_e is related to the open fraction $\gamma_0 = 1 - \sigma_0 / A$, where σ_0 is the cross-sectional area of the grid and A is the surface area of the grid sphere, by the grid absorption efficiency,

$$\eta \equiv \frac{1-\gamma_e}{1-\gamma_0}; \tag{3}$$

i.e., $\eta = \sigma_g / \sigma_0$, where σ_g is the cross section for absorption of ions by the grid. Dolan has given an expression for γ_e / γ_0 which depends on the grid wire spacing and diameter and for which a typical value of $\eta \cong 1.35$.[37] On the other hand, Miley, et al., have given fits of empirical data to Paschen curves, supported by theoretical arguments, which give typical $\eta \cong 0.1$.[3]

The current which is measured experimentally is the power supply current I_S, and it is related to the circulating current by

$$I_0 = \frac{I_S - I_{hv}}{1+\delta} \frac{2\gamma_e}{1-\gamma_e^2}. \tag{4}$$

where δ is the secondary electron emission coefficient and I_{hv} is the secondary photoelectric emission rate. For the nominal operating current $I_S = 50$ mA, values of I_0, along

Table I. Geometric transparencies and nominal circulating currents for the two cathode grids ($I_S = 50$ mA, $\eta = 1$).

	γ_0	I_0
15 cm grid	0.964	1.24 A
23 cm grid	0.976	1.87 A

with γ_0, are given in Table I for the two cathode grids for the case $\eta = 1$, using, from the interferometry voltages of $1 - 2$ kV, $\delta = 0.1$,[28, 38] and assuming $I_{hv} \ll I_S$. These values of I_0 correspond also to $\eta = 0.56$ for the case $\delta = 1$.[39] Also of interest is the electron space charge current into the anode I_e; this current flows in one direction only and, although I_S has other contributions, the net result is

$$I_e = I_S. \tag{5}$$

It is these primary currents I_0 and I_e, then, which anchor the steady state 1-D model. This model consists of the Poisson equation,

$$\rho^{-2} \frac{d}{d\rho}\left(\rho^2 \frac{d\phi}{d\rho}\right) = \frac{n_0 - n_1}{n_g}, \tag{6}$$

and a prescription for the distribution over energy of the charge carriers.[19, 12-14, 17, 31-33] Here ρ and ϕ are the dimensionless radius and potential, respectively, defined as

$$\rho \equiv \frac{r}{r_g}, \quad \phi \equiv \frac{V}{V_g}, \tag{7}$$

where r and V are the radial position and electrostatic potential, respectively, and the subscript g denotes values at the cathode grid; n_0 and n_1 are the number densities of charge carriers from the $\phi = 0$ and 1 electrodes respectively; and

$$n_g \equiv \frac{\epsilon_0}{r_g^2}\left|\frac{V_g}{q_e}\right| = 5.53 \times 10^8 \frac{|V_g \text{ kV}^{-1}|}{(r_g \text{ cm}^{-1})^2} \text{ cm}^{-3} \tag{8}$$

is a characteristic density, in which ϵ_0 is the free-space permittivity and q_e the electronic charge. It is of note here that this formulation is applicable to grid voltages of either polarity,[13] and that it is convenient in some calculations to reference the potential to the anode.[19] However, for the explicit treatment here: $V_g < 0$; $\phi \equiv 0$ at the anode; the subscript "0" will denote ions; the subscript "1" will denote electrons; and the index $i = 0,1$ will be used to denote either (or both). The ion charge is taken to be $q_0 = -q_1 = |q_e|$. We introduce two dimensionless currents, the mono-energetic perveance,[19]

$$K_i \equiv \frac{I_i}{4\pi \epsilon_0 |V_g|^{3/2}}\left(\frac{m_i}{|2q_e|}\right)^{1/2}, \tag{9}$$

and the general form

$$k_i \equiv \frac{K_i}{C_i}; \tag{10}$$

where C_i is a distribution function normalization factor,[13] and current-normalized densities $\hat{n}_i$, which are related to the Poisson densities by

$$\hat{n}_i = k_i^{-1}\frac{n_i}{n_g}. \tag{11}$$

The procedure then is to form a pair of functions $\hat{n}_0(\rho,\phi)$ and $\hat{n}_1(\rho,\phi)$, considering ρ and ϕ as independent variables, by specifying constraints on the distribution over energy of each species of particle. This fundamentally provides a relation between ϕ and the equations of motion.[40] Defining the (conserved) angular momenta,

$$L_i = m_i \upsilon_{t,i} r ,$$ (12)

the (conserved) total energies,

$$E_i = q_i V(r) + \frac{1}{2} m_i \upsilon_{r,i}^2 + \frac{L_i^2}{2m_i r^2} ,$$ (13)

the normalized energies and momenta,

$$\varepsilon_i \equiv \frac{E_i}{q_i V_g} , \quad \lambda_i^2 \equiv \frac{L_i^2}{2m_i r_g^2 E_g} ,$$ (14)

and the integral-normalized distribution functions f_0 and f_1, the normalized densities are

$$\hat{n}_i(\rho,\phi) = \int d\varepsilon_i \int d\lambda_i f_i(\rho,\phi,\varepsilon_i,\lambda_i) ,$$ (15)

where: υ_r and υ_t are the radial and transverse velocities, respectively; $E_g \equiv |q_e V_g|$; and the $\varepsilon_i , \lambda_i$ are to be implicitly constrained so that the kinetic energies, $\phi - \varepsilon_0$ and $\varepsilon_1 - \phi$, and the radial kinetic energies $|\phi - \varepsilon_i| - \lambda_i^2 \rho^{-2}$, remain nonnegative.[13] Using these functions $\hat{n}_i$, solutions $\phi(\rho)$ of the Poisson equation are obtained for values assigned to the k_i, resulting in density profiles $n_i(r) = n_g k_i \hat{n}_i[\rho,\phi(k_i,\rho)]$. In the context of kinetic theory, the distribution functions f_i provide solutions to the Vlasov equation.[17]

It should be noted that while the solutions of the Poisson equation depend on the circulating current through Eq. (9), these solutions may be obtained without explicit specification of the current, or of the cathode voltage or radius. Given a solution $\phi(\rho)$, the physical number densities n_i require specification of V_g and r_g, but not m_i, and the circulating current I_0 requires specification of V_g and m_0, but not r_g. The relation between I_0 and $n_0(r_g)$ is

$$\frac{I_0}{4\pi r_g^2 |q_e|} = n_g k_0 \int d\varepsilon_0 \int d\lambda_0 f_0(1,1,\varepsilon_0,\lambda_0) \upsilon_{r,0}(1,1,\varepsilon_0,\lambda_0)$$ (16)

and that between I_e and $n_1(r_a)$

$$\frac{I_e}{4\pi r_a^2 |q_e|} = n_g k_1 \int d\varepsilon_1 \int d\lambda_1 f_1(a,0,\varepsilon_1,\lambda_1) \upsilon_{r,1}(a,0,\varepsilon_1,\lambda_1)$$ (17)

where r_a is the anode radius and $a \equiv r_a / r_g$; the normalization factors C_i are evaluated from these expressions as $C_i = \sqrt{2E_g / m_i} \int d\varepsilon_i \int d\lambda_i f_i \upsilon_{r,i}$.[13]

In the simplest case, the particles are mono-energetic and have purely radial motion. This is the original model due to Hirsch and Porter.[12, 19] All ions have $\varepsilon_0 = 0$, all electrons have $\varepsilon_1 = 1$, and the densities are simply related to the space potential through conservation of energy, becoming singular at the source electrodes, where the velocities vanish, and at the origin. In this case, there are clearly defined limits, imposed by the space charge, on the magnitude of the currents. Given a ratio of electrode radii a, there is a unique solution for which both currents are space-charge limited.[8, 19]
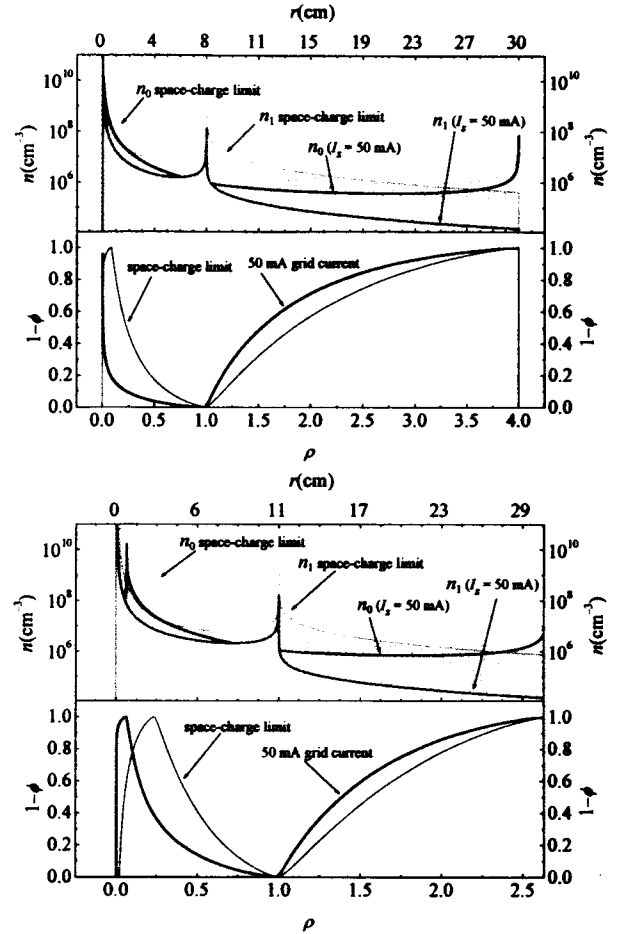

FIG. 6. Mono-energetic solutions of the IEC Poisson equation.

For the 15 cm grid, $a = 4$ and this limits the ion current between r_a and r_g to $K_0 = 0.296$, corresponding to 2.29 mA for Ar ions at $V_g = -1$ kV. For the experimental case, however, $I_e = 50$ mA ($K_1 = 0.024$), giving $K_{0,max} = 0.0949$ and $I_0 = 0.734$ mA. In either case, K_0 is continuous across the cathode, and K_1, which need not be, takes up a new value interior to the cathode based on this K_0, and so on.[19] The densities and potential for the case of space charge limit on both currents, and for the case of limiting currents subject to $I_e = 50$ mA, are given in Fig 6. The free-space density singularities interior to the cathode have been called virtual electrodes, and it is of note that, although the n_i become singular at all source electrodes, these singularities are integrable. The mean density in a spherical shell $|\rho - \rho_s| << \rho_s$, where ρ_s is the radius of the singularity, is

$$\bar{n}_i(\rho - \rho_s) = \frac{4\pi}{\frac{4}{3}\pi(\rho^3 - \rho_s^3)} \int_{\rho_s}^{\rho} d\rho' \rho'^2 n_i(\rho') ,$$ (18)

in which $n_i(\rho) = n_g K_i \rho^{-2} \phi^{-1/2}$ and $\phi \cong (9K_i/4)^{2/3} (|\rho - \rho_s|/\rho_s)^{4/3}$,[8, 19] giving

$$\bar{n}_i(\rho - \rho_s) \cong n_g \left[\frac{\sqrt{12} K_i}{\rho_s^2 |\rho - \rho_s|} \right]^{2/3} .$$ (19)

Eq. (19) is used in computing the mean densities for Fig. 6, given in Table II below. Also of note is that the data plotted

in the figure are cut off arbitrarily at small ρ; in the model, successive interior singularities exist for indefinitely decreasing ρ (and increasing ratios of virtual electrode radii).

The mono-energetic space charge limit on density may be effectively circumvented by dispersion of the particle energy, and these dispersed distributions also generally remove the electrode singularities. Rectangular distribution functions, based on the Heaviside unit step function h, have been examined by Dolan, et al.,[13] and others.[14, 17, 31–33] The case[13]

$$f_{i,H}(\rho,\phi) \equiv$$

$$n_g k_i h_i(\varepsilon_i,\lambda_i) \rho^{-2} \left[|\phi(\rho) - \varepsilon_i| - \lambda_i^2 \rho^{-2} \right]^{-1/2}, \quad (20)$$

where

$$h_i(\varepsilon_i,\lambda_i) \equiv$$

$$h(\varepsilon_i - \varepsilon_{i,\min}) h(\varepsilon_{i,\max} - \varepsilon_i) h(\lambda_{i,\max} - \lambda_i), \quad (21)$$

is plotted in Figs. 7(a) and (c) for the 15 cm grid, using

$$\varepsilon_{0,\min} = \varepsilon_{1,\min} = 0$$

$$\varepsilon_{0,\max} = \varepsilon_{1,\max} = \lambda_{0,\max} = \lambda_{1,\max} = 1 \quad (22)$$

Physically, Eq. (20) represents an even distribution of ion birth sites. The particles take up orbits in which they oscillate between radii which share a common potential. Thus the range of particle energies at a point is constrained only by the local potential, i.e., low energy ions are absent where $1 - \phi$ is large and low energy electrons are absent where ϕ is large. However, in contrast to density profiles from these distribution functions given for cylindrical geometry in Ref. 13, the n_i from Eq.(20) in Fig. 7 remain singular at the origin, increasing like ρ^{-1} (ϕ constant). This singularity may be removed by thermalizing the angular momentum. Mathematically the singularity is due to convergence of particles at the origin and these particles must have $\lambda_i \to 0$. If the distribution function vanishes for $\lambda_i \to 0$, which is a property of thermal distributions, the $n_i(0)$ remain finite. This is illustrated in Fig. 7 as well, which also plots solutions using the parabolic distribution function,

$$f_{i,L}(\rho,\phi) = \lambda_i f_{i,H}(\rho,\phi) \frac{C_{i,H}}{C_{i,L}}, \quad (23)$$

where $C_{0,H}$ is given explicitly in Ref. 13 (there called C_i), and $C_{1,H}$ and $C_{i,L}$ are derived in the same way [from Eqs. (15) and (16)]. The step function limits are those of Eq. (22). The distribution over kinetic energy for Eq. (23) is sensibly identical to that of thermal equilibrium at high temperatures, except that it is truncated by the step functions where the kinetic energy equals the local potential ($1-\phi$ for $f_{1,L}$). The mathematical form of $f_{i,L}(\varepsilon_i) = \int f_{i,L}(\varepsilon_i,\lambda_i)d\lambda_i$ is, within the ε_i limits, generally parabolic, although for both the rectangle and the parabola functions, limits on λ_i may modify the shape.

In Fig. 7, as in the experimental case of Fig. 6, the currents have been maximized subject to the constraint $I_S = 50$ mA. For the dispersed distributions, however, the limiting currents are not defined as precisely as with the mono-energetic case. The general procedure adopted here to determine a value for $k_{i,\max}$ is to increase k_i until the
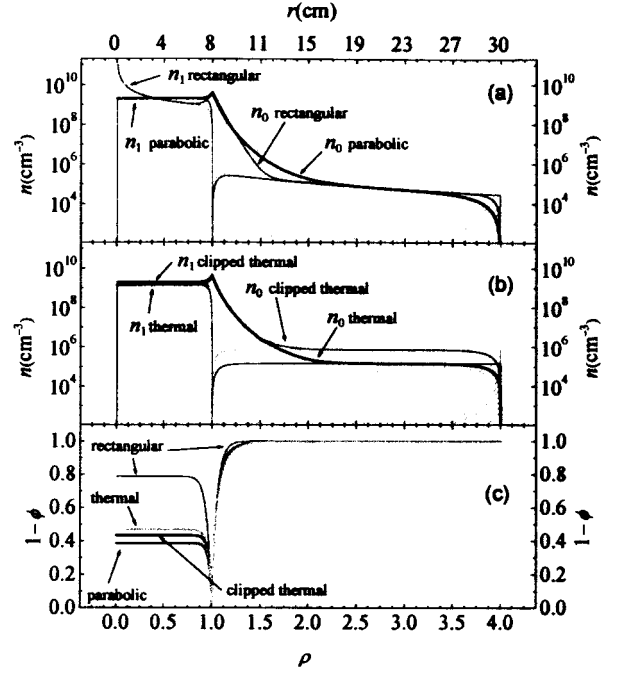

FIG. 7. 15 cm grid density and potential profiles for kinetic solutions using dispersed distributions ($\eta = 1$, $\delta = 0.1$). (a) gives n_i for the rectagular functions Eq. (20) and the parabolic functions Eq. (23); and (b) gives n_i for the thermal functions Eqs. (24) and (25). The two cases in (b) are for the superposition of broad (full) and narrow (clipped) step functions on the thermal distributions. (c) gives $1-\phi$ for all cases. In all cases, $I_S = 50$ mA, $V_g = -1$ kV, and the electron and ion densities are essentially equal for $\rho <= 0.8$.

numerical integration of the Poisson equation begins to fail, where a failure is defined in terms of a merit function for the integration. This merit function is based on the degree to which the target boundary conditions are met and the degree to which the target boundaries (in ρ) themselves are attained, and an arbitrary upper limit on the merit function of $\cong 0.01$ was used. The numerical integration is performed by the shooting method using an adaptive step size Runge-Kutta algorithm,[41] and the integration proceeds either in a single radial direction, starting from an electrode, or, for high densities, in both radial directions, starting from a variable inter-electrode or intra-cathode ρ. The boundary conditions are $\phi'(0) = \phi(a) = 0$, $\phi(1) = 1$, where the prime denotes differentiation with respect to ρ. In Fig. 7, then, Eq. (5) is used to set k_1 for $\rho > 1$, Table I is used to set k_0 (same for all ρ), and iterative integration is used to maximize k_1 for $\rho < 1$. The resulting current parameters and mean densities are given in Table II, along with values from analogous calculations for the 23 cm grid. To the extent that the exterior region is not of interest, the only requirement imposed by the exterior k_1 is that it be compatible with k_0 for a given a.

For comparison, Figs. 7 (b) and (c) give profiles for the thermal distribution functions:

$$f_{i,T}(\varepsilon_i,\lambda_i) =$$

$$\frac{K_i}{C_{i,T}} n_g h_i(\varepsilon_i,\lambda_i) \lambda_i \rho^{-2} \left(|\phi - \varepsilon_i| - \frac{\lambda_i^2}{\rho^2} \right)^{-1/2} \times$$

7

$$\exp\left\{-\left[\frac{|\phi-\varepsilon_i|}{\varepsilon_{r,i}}-\frac{\lambda_i^2}{\rho^2}\left(\frac{1}{\varepsilon_{r,i}}-\frac{1}{\varepsilon_{t,i}}\right)\right]\right\}, \tag{24}$$

where

$$\varepsilon_{r,i} \equiv \frac{kT_{r,i}}{E_g} \quad, \quad \varepsilon_{t,i} \equiv \frac{kT_{t,i}}{E_g}, \tag{25}$$

and $T_{r,i}$ and $T_{t,i}$ are the radial and transverse temperatures, respectively. In the figures, and in all the work here, $T_{r,0}=T_{t,0}$ and $T_{r,1}=T_{t,1}$ are set to give mean kinetic energies $\bar{U}_i$, at a given ρ,ϕ, equal to those of the rectangular distributions Eqs. (20-22):

$$\bar{U}_{i,T} = \bar{U}_{i,H}. \tag{26}$$

Two version of the thermal functions are plotted, one using "full" thermal distributions with $\varepsilon_{0,\min}=-1$, $\varepsilon_{1,\max}=2$, and one using truncated, or "clipped," distributions with $\varepsilon_{0,\min}=0$, $\varepsilon_{1,\max}=1$; in both cases, the limits are otherwise as given in Eq. (22). For the full thermal distributions the limits are sufficient, for the temperatures here, that $\bar{U}_i=3kT_i/2$ to good approximation, and for the clipped distributions, a bisection routine is used to find the temperatures, generally giving $T_i>2\bar{U}_i/(3k)$. The currents and mean densities are listed in Table II.

Physically, the full thermal distributions have particles with energies unbounded by the local potential, but this is largely inessential to the treatment here. The fraction of the ion population with $U_0>|q_eV|$, or of electrons with $U_1>E_g-|q_eV|$, is typically ≈ 0.1 and, as shown in the figure, the results are very similar for both the clipped and full distributions. The key feature of the rectangular $\hat{n}_i(\rho,\phi)$ is that they decrease as ϕ approaches the potential of the source electrode ($\hat{n}_0$ decreases away from the cathode, and vice versa) because the range of kinetic energies available decreases. The decrease in kinetic energy range occurs at high energies and consequently $\bar{U}_i$ also decreases. In preserving $\bar{U}_i$, this feature of the rectangular distributions is transferred to the thermal distributions, and as a result, the ion temperature decreases and the electron temperature increases in moving away from the cathode (potential).

The densities for the distributions in Fig. 7, while larger than the mono-energetic densities, remain insufficient to explain the microwave results. Transverse profiles from the solutions of Table II are given in Fig. 8. These profiles are based on a model of the microwave beam having a step-function radial profile and a Gaussian-beam axial profile; the central radius, or "waist," is 0.7 cm and the radius at the grid is 1.0 cm, giving a Rayleigh range $\cong r_g$. The mean areal densities from these transverse profiles are of order 10^{10} cm^{-2}. Incrementally higher densities are possible with $k_0=k_1$; e.g., for the parabolic functions, the maximum current is near $k_0=k_1=1000$ and gives, for the 15 cm grid, $\bar{n}_0=2.55\times10^9$ cm^{-3}, $\bar{n}_1=2.03\times10^9$ cm^{-3} (cf. Table II), $I_0=1.93$ A, $\eta=0.357$, and the external solution is valid for $I_S=50$ mA. However, the ion and electron densities from these kinetic solutions are systematically disparate where the electric field is strong, near the grid, and, as pointed out in Ref. 28, such disparity is limited by the cathode voltage. In particular, Gauss's law requires (*)

Table II. Interior parameters ($\rho<1$) for Figs. 6 and 7, and for calculations for the 23 cm grid analogous to the cases in Fig. 7. The mean densities $\bar{n}_i$ are in units of 10^6 cm^{-3}. For the mono-energetic case, $C_i=1$, and $I_0=0.734$ and 1.93 mA, respectively, for the two grids (1 kV Ar).

Grid	para-meter	mono-energetic	rectangular	parabolic	clipped thermal	thermal
15cm	k_0	0.0949	241	641	1544	2303
	k_1	0.00987	65	1300	2300	2750
	$\bar{n}_0$	2.85	1529	2140	2140	1682
	$\bar{n}_1$	2.85	1051	1770	1729	1276
23cm	k_0	0.250, 0.00565	363	967	2329	3473
	k_1	0.0567	20	850	1500	3100
	$\bar{n}_0$	3.97	462	1044	1014	984
	$\bar{n}_1$	3.97	175	813	761	753

$$\int_0^1 d\rho\,\rho^{-2}\int_0^\rho d\rho'\,\rho'^2\left[n_0(\rho')-n_1(\rho')\right]\leq n_g. \tag{27}$$

For the 15 cm grid at 1.74 kV, for example, the uniform net density limit is $\cong 10^8$ cm^{-3}. Also of note in Fig. 8 is that for all of the kinetic solutions N decreases monotonically with increasing x.

To further increase the densities, then, we explicitly invoke, to varying degrees, the plasma approximation, replacing the kinetic electron density $\hat{n}_1$ with a quasi-neutral density $\bar{n}_1$ defined as

$$\bar{n}_1 \equiv (1-v)\hat{n}_0 + v\hat{n}_1, \tag{28}$$

where v is an arbitrary neutrality parameter. For $v\to0$ and $k_0=k_1$, Eq. (28) reduces to the conventional plasma approximation.[40] However, while using $\bar{n}_1$ with the distribution functions Eqs. (22)-(24) permits high intra-cathode densities, continuity of I_0 at the cathode requires also high ion density exterior to the cathode, where the
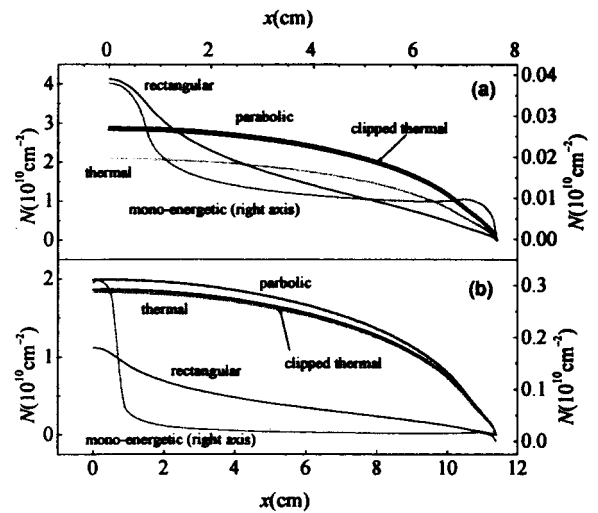

FIG. 8. Transverse profiles of kinetic solution data for (a) the 15 cm grid and (b) the 23 cm grid. All profiles except the mono-energetic solutions are referred to the left ordinate axis. The units are 10^{10} cm^{-2}.

plasma approximation is untenable because of the constraint on I_e. These high exterior densities are ordinarily associated with small values of a,[8] and this ratio is fixed here by the experiment. Mathematically consistent solutions may be formed in this case by $\varepsilon_{0,min} > 0$, which, physically, removes those ions with sufficient energy to approach the anode and increases the concentration of ion space charge near the cathode.

For the thermal functions, the high currents at the cathode may be markedly reduced while preserving the interior densities by truncation of the distribution at the low energy limit, but this truncation is much less effective for the parabolic functions. This is significant because, for both the thermal and the parabolic functions, high currents at the cathode result in small values of η, from Eq. (3). The truncation $\varepsilon_{0,max} < 1$ is thus used here to calculate low-current thermal solutions with $\eta \approx 1$, a relation discussed further in Sect. VI.

In treating the quasi-neutral cases, then, the energy and angular momentum limits will by default be those of Eq. (22) except that $\varepsilon_{0,min} = 10^{-3}$, and, for the thermal case, $\varepsilon_{1,max} = 2$. Where the limits differ from these values, as with the low-current thermal solutions, they will be given explicitly. Also, for the exterior solution, because of the high ion densities some measure of neutrality is imposed on the thermal electron currents by using $\bar{U}_{1,T} = \bar{U}_{0,H}$ in $\hat{n}_{1,T}$ ($\rho > 1$).

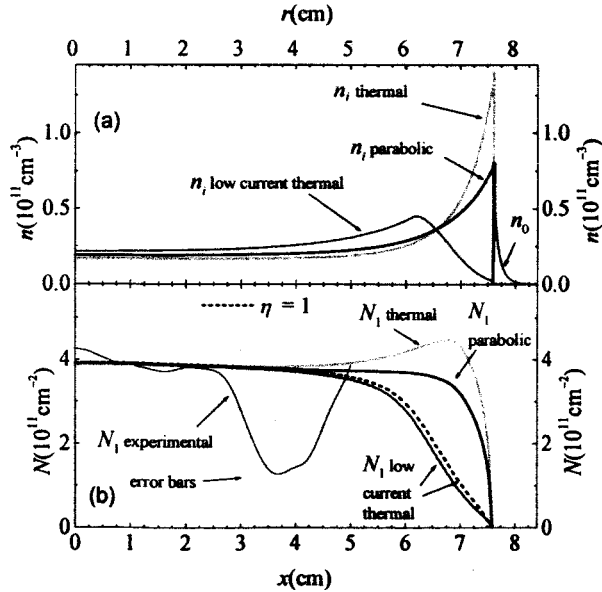Fig. 9 gives radial and transverse profiles from

solutions in the plasma approximation and Table III lists parameters used in these solutions. The radial densities have maxima at or near the cathode, and the currents are chosen to give mean areal densities comparable to those of an experimental transverse profile from Fig. 3. This experimental profile is also shown in Fig. 9, where it has been folded about a best-fit symmetry axis near the nominal x = 0 and averaged over $\pm x$ using cubic spline interpolation. Additional folded profiles from the measurements are given in Fig. 10, along with other selected solutions from the model in the plasma approximation; theoretical parameters are given in Table IV. In these cases, the ratio $k_0 / k_1 > 1$ and the parameter $v > 0$ are used to determine the shape of the transverse profile near the cathode. Although the measurement uncertainties qualify the agreement, these calculations demonstrate quantitative consistency between the 1-D model and the microwave measurements, particularly with respect to features (1) and (2) listed at the close of Sect. 3.

With respect to the eccentric minima, item (3), these dispersed solutions do not exhibit local minima, and this is
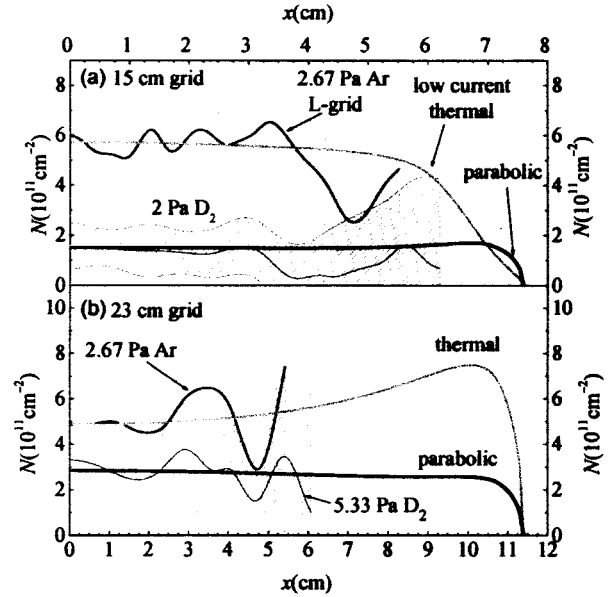

FIG. 10 Comparison of experimental and theoretical transverse profiles in the plasma approximation for (a) the 15 cm grid and (b) the 23 cm grid. $\varepsilon_{0,max} = 0.65$ for the low-current thermal case. The measurement cases, identified by pressure, are, from top to bottom, those of Figs. 3(c), 4(a) (explicit error bars), 3(d), and 4(b) (explicit error bars), respectively. (label error bars)

FIG. 9. Radial (a) and transverse (b) profiles for the 15 cm grid in the plasma approximation. $V_g = -1.48$ kV, $v = 0.004$ in all cases. $\varepsilon_{0,max} = 0.65$ for the low-current thermal case. Shown in (b) only is a second low-current thermal case (broken line) with $\eta = 1$ ($\varepsilon_{0,max} = 0.6671$). The experimental case is that of Fig. 3 (b).

Table III. Parameters for the theoretical cases in Fig. 9.

	thermal	low-I thermal	parabolic
$k_0 (10^4)$	3.223	1.961	0.8537
$k_1 (10^4)$	3.195	1.960	0.8500
I_0 (A)	46.7	0.780	29.7
η	0.027	1.57	0.042

Table IV. Parameters for the theoretical cases in Fig. 10.

$\rho < 1$	15 cm		23 cm	
	low-I	parabolic	thermal	parabolic
$k_0 (10^4)$	4.302	0.375	9.548	1.4572
$k_1 (10^4)$	4.300	0.360	9.530	1.4470
I_0 (A)	1.01	23.6	78.0	37.9
η	1.22	0.053	0.024	0.050
v	0.002	0.01	0.0002	0.004
$\bar{n}_0 (10^{10} cm^{-3})$	4.064	1.560	4.039	1.822
$\bar{n}_1 (10^{10} cm^{-3})$	4.058	1.506	4.031	1.810

emphasized by the example in Fig. 9. In fact, the implication of the pronounced minima in Figs. 3 (a) and (b) is that there are substantial local gradients in the radial density, suggestive of a virtual electrode. For this reason, solutions with inflections in the potential, like the mono-energetic cases, are of interest. However, unlike the mono-energetic cases, these solutions must also have flat central profiles and high interior densities. The flat center may be retained in a quasi-mono-energetic solution by appropriate choice of the limiting angular momentum, and the density may then be increased by superposing quasi-neutral populations from Eq (28). Examples of this are given in Fig. 11 and Table V. The potential profiles in the figure are determined by narrow parabolic distributions having $\Delta\varepsilon = 10^{-5}$ and $\lambda_{max} = 0.3$, and the densities are largely determined by the thermal distributions. For simplicity, $k_0 / k_1 = 1$ and $v = 0$ for the thermal functions. The potentials ϕ in Fig. 11 are double-welled and have local minima at the "virtual anodes" of 4.04 and 5.701 $\times 10^{-3}$ for the 1.06 kV and 1.48 kV cases, respectively. Thus the virtual anodes are not truly anodes, in the sense that the ions which form them are not bound by them. The ions have sufficient energy to breach the potential barrier and therefore the ion currents must be continuous across the anode. For $\rho > 1$, the parabolic ion distribution is shifted to accommodate a so that, in this case, $f_{0,L}$ is not strictly continuous at the cathode, although $f_{0,T}$ and I_0 are. Also shown in Fig 11 are the folded profiles from Figs. 3(a) and (b). The double-well solutions are qualitatively similar and have appropriate mean densities, but the experimental minima are more pronounced than those of the calculations. It is of note in this regard that calculations of the transverse profiles of these double-well solutions which use high spatial resolution (<1 mm) do not differ dramatically from those given in the figure.

One feature of the dispersed distributions which is counter to that found in the mono-energetic case is the concentration of ion space charge at the cathode, and this is true of both the kinetic and the quasi-neutral solutions. For the low-current thermal cases, this peak in the ion density is moved radially inward from the cathode, as in the total density of Fig. 11(b). It is worth mentioning in this connection that calculations from a Berkeley Particle-In-Cell/Monte Carlo code have shown also an intra-cathode ion density peak, which is attributed to thermal effects,[1] although these calculations do not give flat centers (nor exterior peaks). Also of note is the intra-cathode maximum in cylindrical geometry illustrated in Ref. 13 (cf. Fig. 5); in this case, the shift in the maximum, as compared with Fig. 7, is due to limits on the angular momentum. More generally, the dispersed distributions have the property, with limits on ε_i and λ_i tending to exception, that the shape of the curve $\hat{n}_0(\rho)$ follows qualitatively that of $\phi(\rho)$, and $\hat{n}_1(\rho)$ that of $1-\phi(\rho)$.

V. NEUTRON MEASUREMENTS

D-D fusion neutron emission rates $\dot{S}$ were measured using two Eberline Swendi-II ^{3}He neutron detectors. The calibration constant furnished by the
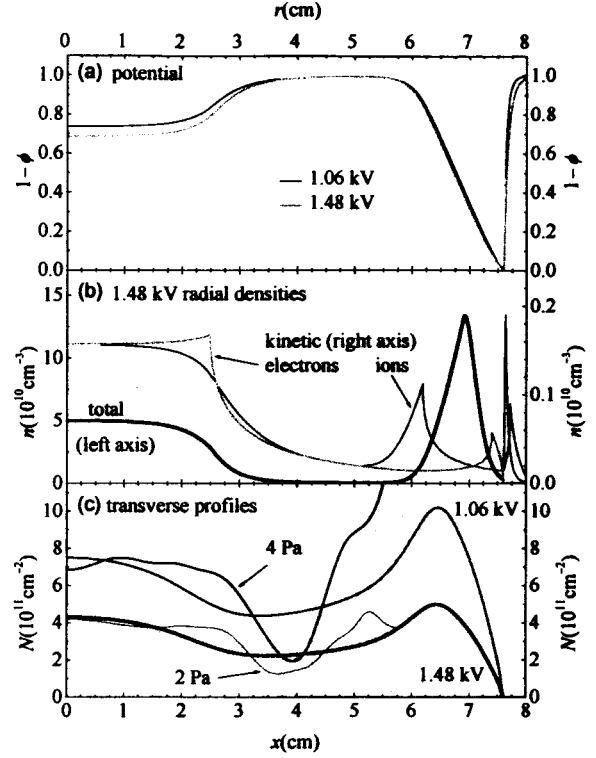

FIG. 11 Potential (a), radial density (b), and transverse density (c) profiles from double potential well solutions using quasi-mono-energetic parabolic functions and low-current neutral thermal populations. $v = 0$ for $\rho < 1$ ($v = 1$ for $\rho > 1$), $\Delta\varepsilon_{i,L} = \varepsilon_{i,L,max} - \varepsilon_{i,L,min} = 10^{-5}$, $\lambda_{i,L,max} = 0.3$. $\eta = 1$ by choice of $\varepsilon_{0T,max}$. The bands in (c) are measured transverse profiles in Ar from Figs. 3(a) and (b), and V_g and I_c for the solutions are taken from these cases.

Table V. Parameters for the theoretical cases in Fig. 11.

	1.06 kV solution		1.48 kV solution	
	$\rho < 1$	$\rho > 1$	$\rho < 1$	$\rho > 1$
k_{1T} (10^5)	1.86	0.039×10^{-5}	0.620	0.023×10^{-5}
k_{1L} (10^5)	181	-	215	-
$\varepsilon_{0L,min}$	0	0.001	0	0.001
k_{0T} (10^5)	1.86		0.620	
k_{0L} (10^5)	301		316	
I_{0T} (A)	1.10		1.00	
I_{0L} (A)	0.114		0.198	
$\varepsilon_{0T,max}$	0.6145		0.6254	

manufacturer for each detector is a dose-equivalent-per-count, integrated over the energy spectrum of the calibration source. The calibration was transferred from a NIST ^{252}Cf standard using an Eberline "rem-ball" detector in conjunction with a Pu-Be source. This constant was used with measurements of the Wendi-II response function $d(E)$ made by Olsher, et al.,[42] to determine the response of the Swendi-II's at the D-D neutron energy, 2.45 MeV. The uncertainty in the Swendi-II calibrations is estimated, from data furnished by Olsher, et al., and Eberline, to be 7.9%. For reference, $\dot{S}$ is one half of the D-D fusion reaction rate.

The Swendi-II detector is housed in a 23 cm diameter cylindrical moderator, 22 cm high, and both detectors were used tangent to the spherical chamber, in the equatorial plane (see Fig. 1). The observation angles θ are measured from the transmitter viewport axis in Fig. 1, and θ_1 was fixed at 35° while θ_2 = 215° and 150°, respectively, for the 15 and 23 cm cathodes. Each detector is attached to a standard meter with a digital display, and the neutron counts S were recorded manually from these displays and logged into the data acquisition system where they are time-stamped. In some cases $\dot{S}$ was recorded directly, but for most of the data (*) the counts S were recorded and converted, post-test, to rates. At the measurement stations, the Swendi-II responses resulted approximately in one count per 1.4×10^4 neutrons. Assuming a $\sqrt{N}$ stochastic signal-to-noise ratio, this gives a statistical error of 8%, equal to the calibration error, at 2.2×10^6 neutrons, which typically corresponds to an integration time of a few seconds. The thickness of the water jacket surrounding the vacuum chamber is 0.97 cm, and a simple calculation of the neutron emission signal attenuation due to this jacket gives a value on the order of a few percent. However, no correction for this effect is included in the data presented here.

Neutron emission data from D-D fusion are given in Fig. 12. The data in Fig. 12(a) are compiled from several different tests overlaid on the time axis, and emission rates are plotted as functions of cathode voltage in Fig 12(b) for both cathodes. The cathode voltage was held approximately constant for the duration of each test in this series and the neutron rates are thus also approximately constant. Emission rates of a few MHz in the range 40 to 60 kV are typical of these devices.[2,4,25-27] The current was about 40 mA for the 15 cm cathode at all voltages, but was reduced somewhat for the 23 cm cathode, because of decreased stability of the plasma at high voltages for this cathode. However, normalization of the neutron rates to the current does not alter the qualitative features of Fig. 12(b). The dependence of $\dot{S}$ on cathode radius for these data is in contrast to that observed earlier at lower voltages in an "emitter-mode"[20] device, which showed an increase (about a factor of 2) in $\dot{S}$ between $a = 4$ and $a = 2$.[4] The pressures in Fig. 12 are from $\cong 0.52$ to 0.4 Pa for both cathodes, compared to a fixed 0.25 Pa pressure in the emitter-mode device.

As with the microwave data, comparison with the model is also of interest for the fusion data, although in this case the parameter space is less restricted, due in part to the absence of spatial resolution. Because of the high voltages, mono-energetic solutions with sufficient current are now possible, and for the dispersed distributions, only kinetic solutions are considered. Also, it should be noted that the visual appearance of the plasma at these voltages differs from that at lower voltages in that the spherical "core" is much smaller and in that distinct radial channels become discernable at grid openings.[22]

To calculate neutron rates from the model, values must be assigned to δ, η, T_2, and the atomic fractions χ_0 and χ_2, defined as
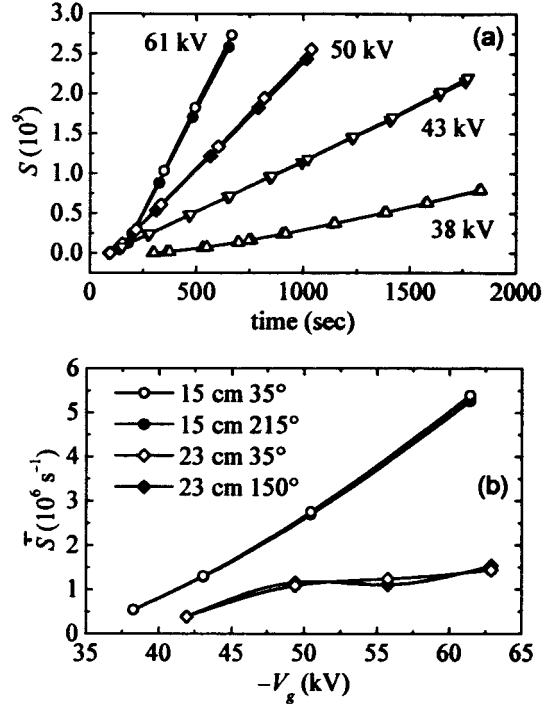

FIG 12. (a) Cumulative neutron counts for two directions for the 15 cm cathode. Open symbols are θ_1, solid symbols are θ_2. (b) average emission rates as functions of cathode voltage, again for two directions, for the 15 cm cathode (upper curve) and the 23 cm cathode (lower curve).

$$\chi_0 \equiv \frac{n_{D^+}}{n_{D^+} + n_{D_2^+}}, \quad \chi_2 \equiv \frac{n_D}{n_D + n_{D_2}}, \quad (29)$$

where $n_{D^+}, n_{D_2^+}, n_D$ and n_{D_2} are the number densities of, respectively, free deuterons, molecular deuterium ions, neutral deuterium atoms and neutral deuterium molecules. The secondary electron coefficient δ depends on the ion energy, and thus on V_g and f_0, and from typical behavior of this coefficient[38] and earlier work,[39] a value of $\delta = 1$ is used here. For the currents I_0 the efficiency is taken to be $\eta = 1$. Both limiting values (0 and 1) of χ_0 are examined, and for convenience we set $T_2 = 10^3$ K and $\chi_2 = 0$. As indicated above T_2 is not known, and by the same token χ_2 may be substantial (certainly it is not categorically negligible, as evidenced by the Balmer-series optical emissions from the plasma), but the target deuteron number density, and thereby the fusion rate, is taken to be proportional to $(2 - \chi_2)T_2^{-1}$, and the results are thus readily generalizable with respect to T_2 and χ_2. Beam-beam reactions are neglected.[4] Given these parameters, kinetic solutions for the experimental conditions of Fig. 12(b) were used to calculate neutron emission rates,[42] and these rates are compared with the empirical rates from the figure, averaged over the two directions, in Table VI. The increase in $\dot{S}$ with increasing χ_0 is due to the increase in the fusion cross section $\sigma_F(E)$ with increasing incident deuteron energy. For the thermal solutions, $\varepsilon_{0,min} = -7$, $\varepsilon_{1,max} = 8$ was used for comparison; with $U_0 \le |q_e V|$ the $\chi_0 = 0$ rates are

11

similar for the thermal and parabolic cases (*). These solutions are discussed further in the following section.

Neutron emission was also observed, at reduced rates, in protium experiments conducted subsequent to operation with deuterium. This emission is attributed to residual deuterium from the vacuum chamber walls and cathode grid (*); the fusion cross section for protium at these energies is negligible. Fig. 13 shows emission rates for the 15 cm cathode for four sets of measurements in protium, sequential in time, made on the 2nd, 3rd, 12th and 15th days, respectively, following termination of deuterium flow through the chamber. No operations were conducted on the intervening days. For comparison, background rates, measured with the high voltage switched off, are typically of order 10^{-4} MHz.

Significant anisotropy in neutron emission was observed in the residual experiments. The anisotropy Δ is quantified here as the fractional difference between the two directions,

$$\Delta \equiv 2\left[S(\theta_1) - S(\theta_2)\right]/\left[S(\theta_1) + S(\theta_2)\right], \tag{30}$$

and is plotted in Fig. 14 for the individual measurements from which Fig. 13 was compiled, as well as for an analogous set of measurements made with the 23 cm cathode. The mean anisotropies were 45% and 16% for the 15 and 23 cm cathodes, respectively. By comparison, the measurement error for this data δS, computed as the root-sum-square of the calibration error and the statistical error at each point, has mean values of 12.6% and 8.7%, respectively. A similar analysis was performed for a collection of deuterium data (including that in Fig. 12) and these results are also shown in the figure. For normal deuterium operations, the anisotropy in neutron emission is within the measurement error. Since the cathode grid itself is somewhat anisotropic, both by design and construction, these results suggest that the contribution to $\dot{S}$ of beam-target reactions in the cathode is more significant under the residual conditions. The cathode contribution in normal operations, not addressed in Table VI, is discussed in Ref. 4.

While the IEC device is generally characterized by stable operation, anomalies were observed on occasion. In one of the experiments, emission rates as much as a factor of 2 greater than those of Fig. 12 were measured under nominal conditions approximately identical to those of the figure.
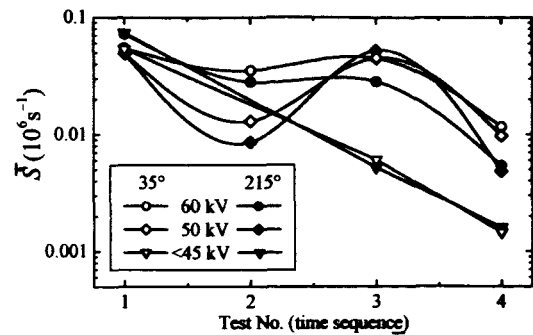

FIG. 13. Residual neutron mean emission rates $\dot{S}$ in two directions during protium operation with the 15 cm cathode.
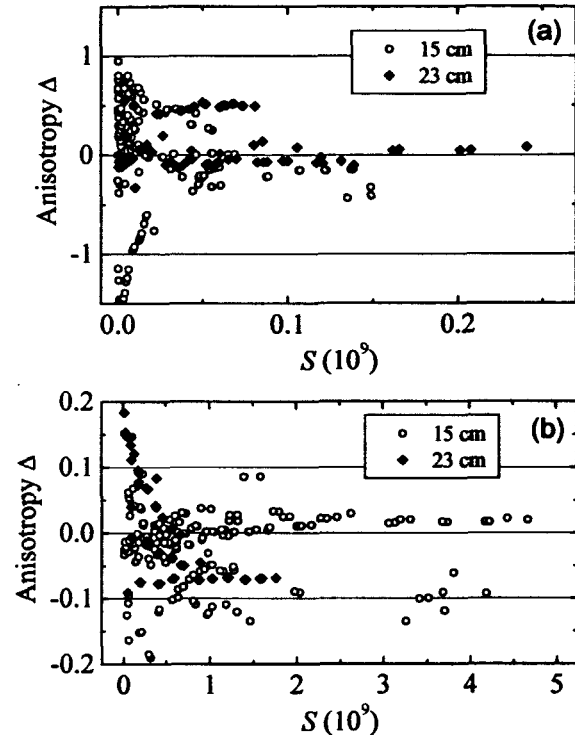

FIG 14. Neutron emission anisotropy for the two cathodes. (a) Residual emission from protium operation. The mean value of $|\Delta|/\delta S$ is 4.39 for the 15 cm cathode and 1.94 for the 23 cm cathode ($\overline{|\Delta|/\delta S}$ = 3.59 and 1.85). (b) Normal deuterium emissions. The mean value of $|\Delta|/\delta S$ is 0.562 for the 15 cm cathode and 0.891 for the 23 cm cathode ($\overline{|\Delta|/\delta S}$ = 0.562 and 0.896); i.e., the anisotropies are within the measurement error.

Table VI. Measured and calculated D-D fusion neutron emission rates for $\delta = \eta = 1$. The measured rates are denoted $\dot{S}$, and the theoretical rates are denoted $\dot{S}_E$, $\dot{S}_L$ and $\dot{S}_T$, respectively, for the mono-energetic, parabolic, and thermal distributions. The experimental conditions, and the measured rates, are those of Fig 12(b), and the theoretical rates have $\chi_2 = 0$, $T_2 = 10^3$ K. The rates are in units of 10^6 neutrons/s.

	V_g(kV)	p(Pa)	I_c(A)	$\dot{S}$	$\dot{S}_E$	$\dot{S}_L$	$\dot{S}_T$	$\dot{S}_E$	$\dot{S}_L$	$\dot{S}_T$
						$\chi_0 = 0$			$\chi_0 = 1$	
15 cm grid	−38.3	0.523	0.573	0.54	0.372	0.109	0.263	5.24	1.83	2.23
	−43.1	0.493	0.545	1.30	0.585	0.170	0.360	6.80	2.43	2.74
	−50.5	0.455	0.572	2.72	1.09	0.333	0.588	10.2	3.79	3.90
	−61.4	0.413	0.573	5.32	2.12	0.672	0.981	14.9	5.91	5.52
23 cm grid	−42.0	0.517	0.652	0.39	0.909	0.272	0.594	11.1	3.92	4.53
	−49.4	0.480	0.616	1.12	1.66	0.495	0.894	15.5	5.66	5.91
	−55.8	0.400	0.529	1.17	1.96	0.588	0.948	15.1	5.68	5.59
	−62.9	0.403	0.452	1.49	3.18	0.807	1.16	17.3	6.68	6.23

12

Similarly, mean emission anisotropies of approximately 24% were noted in deuterium plasmas during one test sequence.

VI. DISCUSSION AND CONCLUSIONS

The electron density profiles measured in the IEC plasmas are generally consistent with dispersed total energy distributions which have thermalized angular momentum, i.e., distribution functions which vanish as the transverse kinetic energy goes to zero. The particular distributions used here are (1) that of thermal equilibrium, optionally truncated by step functions, and (2) a parabolic distribution function, computationally simpler than the thermal case and equivalent to high-temperature equilibrium truncated by the local potential. The magnitude of the mean densities for these distributions is limited by net charge near the cathode to values which are lower that those observed in most cases. For Ar at 1 kV, for example, the disparity is more than an order of magnitude. Solutions of sufficient density, however, are possible using the plasma approximation, and these solutions have transverse profiles which, like the Ar data but unlike the kinetic solutions, tend to increase near the cathode.

Symmetric minima in the measured transverse profiles are observed at about $r_g/2$ for some of the data. This feature is particulary clear for the standard 15 cm grid, a result which may, however, be due more to the transverse scan limits and the measurement uncertainties than to grid size or design. Similar but distinctly broader and shallower minima are predicted by 1-D solutions which superpose low-density quasi-mono-energetic kinetic distributions and high-density neutral thermal distributions. These hybrid solutions exhibit a double potential well in which the inner well has a depth of about 1/3 of the cathode potential. In all the experimental cases, though, it is worth emphasizing that the solutions are not generally determined uniquely by the data, and that where the agreement is limited, as in the hybrid case, a candidate cause is the limitations of the model; the f_i here are significantly restricted in form and are not explicitly coupled to collisional processes in the plasma.

In Figs. 10 and 11, theoretical transverse profiles from the 1-D model are matched to the empirical data. Based on the mean density of charged particles from these solutions and, again, with $T_2 = 10^3$ K and $\chi_2 = 0$, the mean ionization fraction for the Ar plasmas is about $2 - 2.3 \times 10^{-4}$ for either cathode and lower, from $0.3 - 1 \times 10^{-4}$ for the D_2. These values, which include the hybrid case with its substantial radial structure, are very similar to those obtained from the mean measured areal densities assuming a uniform radial distribution.

The effective grid transparency predicted by the high-density (plasma approximation) thermal solutions depends on the lower limit imposed on the total ion energy $E_{0,min}$ (upper bound on ε_0). By reducing the slow, short-trajectory, ion populations near the grid, the current is reduced disproportionately to the total ion population, and absorption efficiencies near unity are possible. For unrestricted energies, both the thermal and parabolic distribution functions result in typical efficiencies of 0.1 to
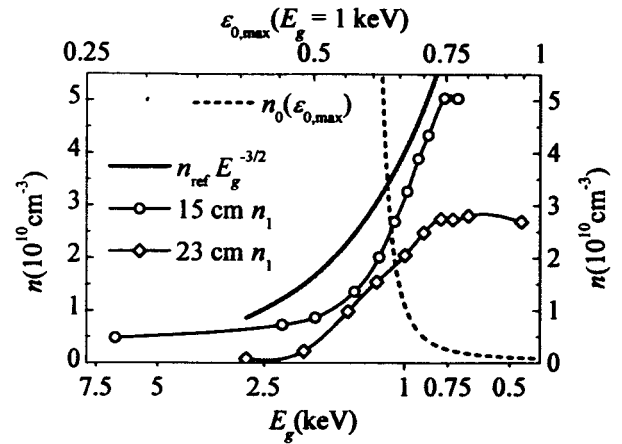

Fig. 15 Electron number density as a function of cathode voltage for the Ar pressure scans. The data are from Fig. 5 and the number densities are calculated for uniform spatial distribution of the electrons. $I_S \cong 45$ mA for all data. The thick curve shows the perveance scaling of density and the broken line, referenced to the top axis, illustrates the dependence of density on the lower bound of ion energy for fixed current in the thermal distributions.

0.015. Exterior to the cathode, it is necessary to impose an upper bound $< E_g$ on the ion energy in order to obtain consistent solutions for the experimental conditions.

In the Ar pressure data of Fig. 5(b), $N_1(x=0)$ increases with decreasing E_g until about 0.75 keV, where $N_1(E_g)$ becomes approximately constant. Fig. 15 shows this explicitly, giving $\bar{n}_1(E_g)$ for the Ar data from both grids in Fig. 5 using a uniform radial profile; the current $I_S \cong 45$ mA. Dispersion of the ion energy due to ionization distribution[20] and charge exchange[44] has been used to explain a dependence of fusion rate density on neutral pressure resembling the $\bar{n}_1$ curves of Fig 15 (cf. Fig. 4 of Ref. 20), and similar considerations apply here. From Eqs. (9)–(11), for a given solution $\phi(\rho)$ and fixed current I_0, the ion density scales as $E_g^{-3/2}$ and this is illustrated in the figure using an arbitrary $n_{ref} = 4 \times 10^{10}$ cm^{-3} keV$^{3/2}$. Assuming that $\bar{n}_1 \cong \bar{n}_0$, which is generally the case for the kinetic solutions considered and necessarily the case for the high-density solutions, $\bar{n}_1$ also will tend to increase with pressure like $E_g^{-3/2}$. However, for the voltages of this data the charge exchange cross section σ_q for Ar$^+$ ions in Ar increases with decreasing energy, increasing by about a factor of 2 (to $\cong 3 \times 10^{-15}$ cm^2) between 2.5 and 0.1 keV.[38] From 2.5 kV down to 0.75 kV the mean ion velocity $\bar{v}_0$ decreases by about a factor of 2 while the neutral number density n_{Ar} increases by about a factor of 10 (see Fig. 5). Thus the charge exchange rate per ion $n_{Ar} \sigma_q \bar{v}_0$ will increase with decreasing voltage and f_0 will tend to increase at the low energy end. Fig. 15 also gives a plot of $\bar{n}_0(\varepsilon_{0,max})$ for constant I_0 at $E_g = 1$ keV and it is seen that $\bar{n}_0$ decreases sharply as the low energy region is filled. The solutions used are those of the hybrid case from Fig. 11 with $\eta = 1$. Thus for distributions of this kind there are opposing influences on $\bar{n}_1$ with increasing pressure and it is reasonable to expect that a local maximum like that in Fig. 15 would be observed.

13

For the parabolic distributions, on the other hand, variation of $\varepsilon_{0,max}$ (and $\lambda_{0,max}$) is largely ineffective in regulating I_0 independently of $\bar{n}_0$. In this case, as in the thermal case with $\varepsilon_{0,max} = 1$, solutions consistent with the observations require variation of η with cathode voltage and, as indicated, imply small values for this parameter. These two alternatives, high-current/low-energy and low-current/high-energy, may, for a given mean density, be distinguished observationally on the basis of the interior density profile near the cathode. Both n and N in this region are larger for the high-current cases, as illustrated in Figs. 9 and 10.

For the deuterium fusion data, the measured quantity is the total neutron emission rate $\dot{S}$. The measurement of phase shifts below 1 Pa in D_2 was not practical with the current system [e.g., see Fig. 5(c)], and consequently the densities are not directly known. In general though, the kinetic solutions $\phi(\rho<1)$ for the small perveances of the combinations of I_0 and V_g for this data form shallow wells with $V \cong V_g$, and $\bar{n}_0$ in these cases is fairly insensitive to $\bar{n}_1$. The k_1 for the solutions of Table III were chosen to give $\bar{n}_1$ of the same order as $\bar{n}_0$, but the resulting values of $\dot{S}$ are similar in the absence of electrons. The presence of electrons in the solutions does, however, drive the central potential further towards the cathode potential. For the data in the table, $1 - \phi \cong 0.001$ to 0.005 is typical. These shallow wells are consistent with the argument given by Meeker, et al., for low-energy electron populations trapped inside the cathode for ion-injected IEC plasmas (cf. Fig. 14 of Ref. 28).

The low-energy electrons are a source of both atomic and molecular ions. In the range of from $\cong 50$ to 100 eV, from H_2 data[45] and from vibrational state tables for D_2,[46] the cross section for electron impact ionization of D_2 is $\cong 10^{-16}$ cm^2. Also from the tables, the cross section for dissociative ionization of D_2 ($D_2 + e \rightarrow D + D^+ + 2e$) may be estimated as also $\cong 10^{-16}$ cm^2.[46] In these conditions, then, it is expected that both n_{D^+} and $n_{D_2^+}$ may be appreciable, and from Table VI $\chi_0 > 0$ is consistent with the $\dot{S}$ measurements at higher voltages for the 15 cm grid. For these data, though, the calculated values of $\dot{S}$ increase with the grid radius, as shown in the table, and this was not observed. It may also be noted that in the present case ionization by ions is more significant than in Meeker's case, due to the larger cross section. In the range 30 to 60 kV, the cross section for proton impact ionization of H_2 is $\cong 2 \times 10^{-16}$ cm^2, similar to the charge exchange cross section.[47]

The spatial distribution of the fusion rate density $F(\rho)$ in the dispersed solutions is roughly constant inside the cathode and decreases quickly outside the cathode (independently of χ_0). The mono-energetic solutions in contrast have pronounced central peaks. However, all three forms in Table VI have similar cumulative profiles $\zeta(\rho) \propto \int_0^\rho F(\rho')\rho'^2 d\rho'$ and inside the cathode these profiles resemble that given in Fig. 4 of Ref. 4 from proton collimation measurements. For radii well outside the cathode, on the other hand, the empirical profile increases monotonically while the kinetic solutions give flat $\zeta(\rho)$, due to $n_0, \phi \rightarrow 0$. Proton collimation results reported in Ref. 22 show a pronounced central peak in $F(\rho)$. Also, it may be

remarked that, for fixed I_0 in the thermal distributions, the behavior of $\bar{n}_0 (\varepsilon_{0,max})$ suggests that any decrease in $\bar{n}_0$ with increasing E_g which is less marked than the $E_g^{-3/2}$ scaling may be of fusion interest, i.e., due to increase in U_0/E_g.

ACKNOWLEDGEMENTS

[1] R. A. Nebel, L. Turner, T. N. Tiouririne, D. C. Barnes, W. D. Nystrom, R. W. Bussard, G. H. Miley, J. Javedani and Y. Yamamoto, LANL UR 94-1739, Proceedings for NonDestructive Assay and NonDestructive Examination Waste Characterization Conference (Feb. 14-16, 1994).

[2] Yibin B. Gu, Jalal B. Javedani, George H. Miley, Fusion Technology 26, 929 (1994).

[3] G. H. Miley, Y. Gu, J. M. DeMora, R. A. Stubbers, T. A. Hochberg, J. H. Nadler and R. A. Anderl, IEEE Trans. Plasma Sci. 25 (4), 733 (1997).

[4] T. A. Thorson, R. D. Durst, R. J. Fonck, A. C. Sontag, Nuclear Fusion 38 (4), 495 (1998).

[5] George H. Miley, T.H. Bauer, Heinrich Hora and Jon Nadler, in Proceedings of 8th International Conference on Nuclear Engineering, ICONE-8500, (2-6 April, 2000).

[6] J. Sved, Trans. Am. Nucl. Soc. 77, 504 (1997).

[7] M. Nieto, H. Momota, G. H. Miley, Proceedings of the 8th International Conference on Nuclear Engineering, Baltimore MD (April 2-6, 2000).

[8] I. Langmuir and K. B. Blodgett, Phys. Rev. 23, 49 (1923).

[9] I. B. Bernstein, J. M. Greene and M. D. Kruskal, Phys. Rev. 180 (3), 546 (1957).

[10] W. C. Elmore, J. L. Tuck, and K. M. Watson, Phys. Fluids 2 (5), 239 (1959).

[11] R. W. Hockney, J. Appl. Phys. 39 (9), 4166 (1968).

[12] G. D. Porter and E. H. Klevans, Phys. Fluids 14 (2), 428 (1971).

[13] T. J. Dolan, J. T. Verdeyen, D. J. Meeker, and B. E. Cherrington, J. Appl. Phys. 43 (4), 1590 (1972).

[14] K. M. Hu and E. H. Klevans, Phys. Fluids 17 (1), 227 (1974).

[15] M. Rosenberg and N. A. Krall, Phys. Fluids B 4 (7), 1788-94 (1992).

[16] W. M. Nevins, Phys. Plasmas 2 (10), 3804 (1995).

[17] M. Ohnishi, K. H. Sato, Y. Yamamoto, K. Yoshikawa, Nuclear Fusion 37 (5), 611 (1997).

[18] J. H. Nadler, E. D. Yoder, C. Hunsicker and G. H. Miley, 29th Plasmadynamics and Lasers Conference, AIAA-98-2570 (June 15-18, 1998).

[19] R. L. Hirsch, J. Appl. Phys. 38 (11), 4522 (1967).

[20] G. H. Miley, J. Nadler, T. Hochberg, Y. Gu, O. Barnouin, J. Loveberg, Fusion Technology 19, 840 (1991).

[21] R. W. Bussard and Lorin W. Jameson, J. Propulsion and Power 11 (2), 365 (1995).

[22] G. H. Miley, J. Nadler, B. Jurczyk, R. Stubbers, J. DeMora, L. Chacon, and M. Nieto, AIAA-99-2140 (June, 20-23, 1999).

[23] J. Nadler, G. Miley, M. Coventry, Y. Nam, and W. Hammond, AIAA 2000-3608, 36th AIAA/ASME/SAE/ASEE Joint Propulsion Conference and Exhibit (16-19 July, 2000).

[24]Hiromu Momota, George H. Miley and Jon Nadler, AIAA 2000-3609, 36th AIAA/ASME/SAE/ASEE Joint Propulsion Conference and Exhibit (16-19 July, 2000).

[25]Masami Ohnishi, Yasushi Yamamoto, Mitsunori Hasegawa, Kiyoshi Yoshikawa, George H. Miley, Fusion Engineering and Design **42**, 207 (1998).

[26]Masami Ohnishi, Kiyoshi Yoshikawa, Yasushi Yamamoto, Kai Masuda, Hisayuki Toku, Mitsunori Hasegawa, Chikara Hoshino, Takahiro Koyama and Kenji Taruya, Fusion Technology **34**, 1071 (1998).

[27]J. H. Nadler and G. H. Miley, Final Report NASA SBIR Contract #NAS8-99044, NPL Associates, Champaign, IL (June, 1999).

[28]D. J. Meeker, J. T. Verdeyen, and B. E. Cherrington, J. Appl. Phys. **44** (12), 5347 (1973).

[29]J. H. Nadler, Y. B. Gu, and G. H. Miley, Rev. Sci. Instrum. **63** (10), 4810 (1992).

[30]Kiyoshi Yoshikawa, Ken Takiyama, Yasushi Yamamoto, Kai Masuda, Hisayuki Toku, Takahiro Koyama, Kenji Taruya, Hirofumi Hashimoto, Masami Ohnishi, Hiroshi Horiike, and Nobuyuki Inoue, SOFE 99, ISSN 1342-3185 (October 21, 1999).

[31]W. M. Black and James W. Robinson, J. of Appl. Phys. **45** (6) 2497 (1974).

[32]B. E. Cherrington, J. T. Verdeyen, and D. A. Swanson, N.Y. Acad. Sci. Ann. **251**, 139 (1975).

[33]Edward H. Klevans, N.Y. Acad. Sci. Ann. **251**, 190 (1975).

[34]S. C. Brown, *Introduction to Electrical Discharge in Gases*, John Wiley & Sons, N.Y. (1966).

[35]C. C. Dobson, J. E. Jones, and D. G. Chavers, Rev. Sci. Instrum. **75** (3), TBD, (2004).

[36]R. L. Hirsch, Phys. Fluids **11** (11), 2486 (1968).

[37]T. J. Dolan, Plasma Phys. Control. Fusion **36**, 1539 (1994).

[38]S. C. Brown, *Basic Data of Plasma Physics, 1966*, M.I.T. Press, Cambridge MA (1967).

[39]T. A. Thorson, R. D. Durst, R. Fonck, and L. P. Wainwright, Phys. Plasmas **4** (1), 4 (1997).

[40]F. F. Chen, *Introduction to Plasma Physics*, Plenum Press, N.Y. (1974).

[41]W. H. Press, B. P. Flannery, S. A. Teukolsky, and W. T. Vetterling, *Numerical Recipes*, Cambridge University Press, Cambridge MA (1986).

[42]R. H. Olsher, Hsiao-Hua Hsu, A. Beverding, J. H. Kleck, W. H. Casson, D. G. Vasilik, R. T. Devine, LA-UR-99-6551, Los Alamos NL (sub. to Health Phys. J.) (1996).

[43]J.D. Huba, NRL Plasma Formulary, NRL/PU/6790-94-265 (1994).

[44]D. C. Baxter and G. W. Stuart, J. Appl. Phys. **53** (7), 4597 (1982).

[45]http://physics.nist.gov/PhysRefData/Ionization/EII_table.html (Dec. 2003).

[46]R. K. Janev, *Atomic and Molecular Processes in Fusion Edge Plasmas*, Plenum Press, N.Y. (1995).

[47]D. J. Rose and M. Clark, Jr., Plasmas and Controlled Fusion, M.I.T. Press and John Wiley & Sons, N.Y. (1961).